Observational Constraints on Southern Ocean Cloud-phase Feedback

Casey J. Wall[1]*, Trude Storelvmo[2,3], Joel R. Norris[1], Ivy Tan[4]
[1]Scripps Institution of Oceanography, University of California San Diego, La Jolla, CA, United States
[2]Department of Geosciences, University of Oslo, Oslo, Norway
[3]School of Business, Nord University, Bodø, Norway
[4]Department of Atmospheric and Oceanic Sciences, McGill University, Montreal, Canada

Corresponding Author:
Casey J. Wall, cawall@ucsd.edu

Submitted September 4, 2021

Key Points

1. Observations suggest that shortwave cloud-climate feedback is positive over the Southern Ocean
2. Changes in cloud scattering properties arising from ice-to-liquid conversions make a small contribution to the feedback
3. The observational constraints imply a higher climate sensitivity than a recent consensus estimate of cloud feedback

Abstract

Shortwave radiative feedbacks from Southern Ocean clouds are a major source of uncertainty in climate projections. Much of this uncertainty arises from changes in cloud scattering properties and lifetimes that are caused by changes in cloud thermodynamic phase. Here we use satellite observations to infer the scattering component of the cloud-phase feedback mechanism and determine its relative importance by comparing it with an estimate of the overall temperature-driven cloud feedback. The overall feedback is dominated by an optical thinning of low-level clouds. In contrast, the scattering component of cloud-phase feedback is an order of magnitude smaller and is primarily confined to free-tropospheric clouds. The small magnitude of this feedback component is a consequence of counteracting changes in albedo from cloud optical thickening and shifts in the scattering direction of cloud particles. These results indicate that shortwave cloud feedback is likely positive over the Southern Ocean and that changes in cloud scattering properties arising from phase changes make a small contribution to the overall feedback. The feedback constraints shift the projected 66% confidence range for the global equilibrium temperature response to doubling atmospheric CO_2 by about +0.1 K relative to a recent consensus estimate of cloud feedback.

Plain Language Summary

Understanding how clouds respond to global warming is a key challenge of climate science. One particularly uncertain aspect of the cloud response involves a conversion of ice particles to liquid droplets in extratropical clouds. Here we use satellite data to infer how ice-to-liquid conversions affect climate by changing the reflection of incoming solar radiation back to space. We find that the changes in cloud particle size and shape that arise from phase changes make a relatively small contribution to the overall cloud-albedo response to warming. This finding provides new insight about how changes in cloud phase affect climate change.

1. Introduction

The Southern Ocean is one of the cloudiest places on Earth. Vast blankets of low clouds cover the region, and streaks of high clouds form from the continuous churning of weather systems. Collectively these clouds have large radiative effects that shape global climate (Hwang and Frierson, 2013; Kay et al., 2016; Hawcroft et al., 2017).

Southern Ocean clouds are also susceptible to producing cloud-climate feedbacks that have global consequences. For instance, projections from the Coupled Model Intercomparison Project Phase 6 (CMIP6) predict more positive Southern Ocean cloud feedback and higher climate sensitivity than previous assessments (Zelinka et al., 2020). The CMIP6 projections show that Southern Ocean cloud feedback affects climate sensitivity, but the models have large parametric uncertainties that prevent them from precisely predicting this feedback. Previous observational studies have attempted to constrain the feedback, but they have yet to reach a consensus on sign (Ceppi, McCoy, and Hartmann, 2016; Terai et al., 2016; Lutsko et al., 2021). These results indicate that Southern Ocean clouds exert a potentially powerful but highly uncertain feedback on global climate change.

One major component of the feedback uncertainty arises from changes in cloud phase (Storelvmo et al., 2015). As the atmosphere warms, some cloud particles that would have previously been ice will form as liquid instead. These phase conversions change the size and shape of cloud particles, which changes the scattering properties of clouds. Ice-to-liquid conversions also reduce precipitation efficiency, thereby increasing cloud lifetimes. We call these effects the scattering and lifetime components of cloud-phase feedback, respectively. Both are the product of complex interactions among microphysical processes, and thus they are highly uncertain.

In this study we use satellite observations to constrain the scattering component of Southern Ocean cloud-phase feedback. Despite the importance of this mechanism in many climate projections (Ceppi, Hartmann, and Webb, 2016; Tan et al., 2016; Frey and Kay, 2018), observational support for the mechanism has been limited to estimates that do not quantify confidence intervals and do not compare the mechanism to the overall cloud feedback to place it into context (McCoy et al., 2014a; Tan et al., 2019). Here we introduce a method to estimate cloud feedback as a function of cloud-top phase, which facilitates stronger constraints. We first estimate the cloud-phase scattering feedback and the overall temperature-mediated cloud feedback, and then we investigate the implications of these feedbacks for climate sensitivity.

2. Data and Methods

2.1 Observations and Model Output

We extend a method of cloud-feedback analysis developed by Zelinka et al. (2012) to decompose shortwave (SW) feedbacks based on cloud thermodynamic phase. The method is applied to monthly gridded observations from the Moderate Resolution Imaging Spectroradiometer (MODIS) instrument onboard the Aqua satellite (Platnick et al., 2017). MODIS cloud-phase data represent phase at cloud top, and they have a ~90% frequency of agreement with lidar data, which are the most accurate phase retrievals from space (Huang et al., 2016; Marchant et al., 2016). We analyze cloud-fraction histograms partitioned by cloud-top pressure (CTP), optical depth (τ), and phase (Fig. 1a-b). The standard liquid- and ice-cloud histograms have different CTP-τ bins, so some adjacent bins are merged to make the intervals similar. In this step, clouds with CTP $>$ 1000 hPa are reassigned to the 800-1000 hPa bin, and it is assumed that no liquid clouds exist between 50-150 hPa. The standard and modified bin boundaries are listed in Table S1.

We also analyze monthly meteorological data and sea-ice area fraction from ERA5 reanalysis (Hersbach et al., 2020). Three-dimensional temperature, horizontal wind, and vertical wind fields are linearly interpolated to the MODIS grid and to pressure intervals corresponding to the MODIS CTP bins. We also calculate estimated inversion strength, which represents the inversion at the top of the boundary layer (Wood and Bretherton, 2006). The observations and reanalysis data are analyzed between 40°-60°S and from 2003-2019, unless stated otherwise, and the analysis is restricted to ocean gridboxes with monthly sea-ice cover below 1%.

We also use output from 34 CMIP6 global climate models to represent CO_2-forced warming (Table S2). Model simulations are run for 150 years following an abrupt quadrupling of atmospheric CO_2 concentrations relative to preindustrial values ("abrupt4xCO2" experiment). Atmospheric temperatures are linearly interpolated to the MODIS grid and CTP intervals, and then they are averaged over the final 30 years of the simulations. Averages are calculated separately for each latitude, calendar month, and CTP interval. To remove model drift, the temperature response to increasing CO_2 is calculated by subtracting the preindustrial integration ("piControl") from the corresponding parallel abrupt4xCO2 integration. The response of global-mean near-surface air temperature is calculated similarly. Only the first ensemble member from each model is used.

2.2 Radiative Kernels

Cloud-fraction anomalies from each MODIS histogram bin are converted into top-of-atmosphere SW flux anomalies using radiative kernels. The kernels represent how much a unit cloud-fraction change modifies top-of-atmosphere SW flux with all non-cloud factors fixed at climatological values. We calculate the kernels as a function of latitude, longitude, and calendar month following the method of Zelinka et al. (2012), except that we generalize their framework by calculating separate kernels for liquid and ice clouds. The calculations are performed using the Rapid Radiative Transfer Model for GCMs (Clough et al., 2005) with climatological seasonal cycles of humidity from ERA5 and surface albedo from Clouds and the Earth's Radiant Energy System satellite observations (Loeb et al., 2018). We also change the mean cloud-droplet effective radius and ice-crystal effective radius to 14 μm and 35 μm, respectively, to match observed values over the Southern Ocean (McCoy et al., 2014a). Together the cloud histograms and kernels reproduce observed variations of SW cloud radiative effects with an error of ~5% (Appendix A).

Fig. 1c-d shows the spatial and temporal average of the radiative kernels. The kernels have negative values because a larger cloud fraction increases SW reflection to space. They depend relatively strongly on τ, and they depend weakly on CTP because of SW absorption by water vapor. For a given CTP-τ combination, the kernels also depend on cloud phase because ice particles typically backscatter more radiation than liquid droplets (Stackhouse and Stephens, 1991). Changes in any of these cloud properties can therefore contribute to cloud feedback.

2.3 Feedback Analysis

The MODIS histograms and kernels are leveraged to estimate the SW cloud feedback that is directly caused by atmospheric warming. We do not consider SW feedbacks caused by shifts in large-scale circulation because they are thought to be relatively small (Ceppi and Hartmann, 2015). Let i represent any bin in the liquid- or ice-cloud histogram. For a given location and calendar month, the SW feedback from clouds in bin i is

$$F_{SW,i} = \frac{\partial c_i}{\partial T_i} K_i \frac{dT_i}{dT_{2m}} \tag{1}$$

where c_i is cloud fraction, T_i is temperature at the location and vertical level of bin i, K_i is the corresponding element of the kernel, and T_{2m} is global-mean surface air temperature. On the right side of equation 1, the first term is the cloud response to local warming, the second term converts the cloud response into top-of-atmosphere SW flux, and the third term relates local warming to global-mean surface warming. All temperature-dependent terms represent the response to an external climate forcing. The task of quantifying cloud feedback thus reduces to estimating these terms.

We first calculate dT_i/dT_{2m}, which represents the magnitude and vertical structure of atmospheric warming over the Southern Ocean relative to global-mean surface warming. This term is calculated from the CMIP6 projections forced by increasing atmospheric CO_2. The projections of dT_i/dT_{2m} consistently have maximum values in the free troposphere and smaller values in the lower stratosphere and near the surface (Fig. 2). Small stratospheric values are a consequence of larger emissivity from enhanced CO_2 concentrations (Hartmann, 2016), and small near-surface values are a consequence of upwelling ocean currents (Armour et al., 2016). These physical explanations and the consistency among models suggest that the projections of dT_i/dT_{2m} are robust.

The feedback analysis also requires estimates of $\partial c_i/\partial T_i$. This term represents the temperature-driven cloud response to a climate forcing, but it can be estimated from natural variability assuming that cloud-temperature relationships will not substantially change as the climate evolves. This assumption neglects the potential dependence of extratropical cloud feedbacks on the climate state (Bjordal et al., 2020). However, many climate projections suggest that monthly cloud-temperature relationships from natural variability accurately predict extratropical cloud feedbacks (Tselioudis et al., 1998; Gordon and Klein, 2014; Terai et al., 2016; Ceppi, McCoy, and Hartmann, 2016), and observed cloud-temperature relationships are similar in different epochs within the MODIS record (Appendix C). We therefore estimate $\partial c_i/\partial T_i$ from natural variability.

We first estimate $\partial c_i/\partial T_i$ associated with the temperature-mediated feedback. This term represents the overall cloud response to warming, and it is calculated using multilinear regression. Because of the zonal symmetry of the Southern Ocean, regression is performed on data from all longitude points simultaneously. The climatological seasonal cycle is removed from each latitude-longitude gridbox, and data are composited by latitude and calendar month. For each latitude, month, and histogram bin, we calculate a regression model of the form

$$c = \sum_{n=1}^{N} \frac{\partial c}{\partial x_n} x_n + \epsilon \tag{2}$$

where x_n are meteorological predictors, $\partial c/\partial x_n$ are regression coefficients, N is the number of meteorological predictors, and ϵ is the residual. The meteorological predictors include temperature and the three-dimensional wind field at the level of the CTP interval. Estimated inversion strength is also used as a predictor for CTP $>$ 450 hPa. The term $\partial c/\partial T$ therefore represents the cloud response to warming while controlling for wind and inversion strength. On average, the regression model explains 38% of the variance of cloud-induced SW flux anomalies for boundary layer clouds (CTP $>$ 800 hPa) and 18% of the variance for tropopause-level clouds (250 hPa $<$ CTP $\leq$ 350 hPa). The explained variance for boundary layer clouds is similar to that of other observational work that uses different meteorological predictors (Scott et al., 2020). This suggests that the regression model represents cloud-meteorology relationships with skill that is similar to other available methods. Ultimately the cloud-temperature regression coefficients are used to estimate the temperature-mediated feedback following equation 1.

We also estimate the component of the temperature-mediated feedback that arises from changes in low-cloud optical depth. We define low clouds by CTP $>$ 600 hPa, and we apply the method of Scott et al. (2020) to decompose low-cloud fraction anomalies into a component from anomalous cloud amount and a component from anomalous cloud optical properties and CTP. The latter component is regressed on the meteorological predictors to estimate the associated SW feedback. This feedback component is dominated by shifts in optical depth, so we henceforth call it the low-cloud optical depth feedback.

The values of $\partial c_i/\partial T_i$ associated with the scattering component of cloud-phase feedback are estimated from a different procedure. We calculate these terms separately for each CTP bin so that phase conversions happen between clouds at the same vertical level. For a given CTP bin, the proportion of clouds that are liquid is

$$P_{liq} = \frac{C_{liq}}{C_{liq} + C_{ice}}$$

where C_{liq} and C_{ice} are the total liquid- and ice-cloud fractions in the CTP bin. P_{liq} is regressed on the meteorological predictors as in equation 2 to calculate $\partial P_{liq}/\partial T$, where T is temperature in the CTP interval. Changes in C_{liq} and C_{ice} with warming are determined by

$$\frac{\partial C_{liq}}{\partial T} = \frac{\partial P_{liq}}{\partial T}\left(\overline{C_{liq}} + \overline{C_{ice}}\right)$$

$$\frac{\partial C_{ice}}{\partial T} = -\frac{\partial P_{liq}}{\partial T}\left(\overline{C_{liq}} + \overline{C_{ice}}\right)$$

where overbars indicate values from the climatological seasonal cycle. $\partial C_{liq}/\partial T$ and $\partial C_{ice}/\partial T$ are equal and opposite, so they represent a phase change with fixed overall cloud fraction. The values of $\partial C_{liq}/\partial T$ and $\partial C_{ice}/\partial T$ are then distributed among the τ bins in proportion to the climatological distributions:

$$\frac{\partial c_{liq,k}}{\partial T} = \frac{\partial C_{liq}}{\partial T}\frac{\overline{c_{liq,k}}}{\overline{C_{liq}}}$$

$$\frac{\partial c_{ice,l}}{\partial T} = \frac{\partial C_{ice}}{\partial T}\frac{\overline{c_{ice,l}}}{\overline{C_{ice}}}$$

where $c_{liq,k}$ and $c_{ice,l}$ are the liquid- and ice-cloud fractions in τ bins k and l, respectively. By distributing cloud fraction this way we are assuming that for any latitude-month-CTP bin, all ice clouds in the bin have the same probability of undergoing a phase change. Ultimately $\partial c_{liq,k}/\partial T$ and $\partial c_{ice,l}/\partial T$ are used to calculate the cloud-phase scattering feedback following equation 1. An example of this procedure is presented in the Supporting Information.

The cloud-phase scattering feedback is also decomposed into contributions from changes in different optical properties. The total cloud-phase scattering feedback for a given latitude, month, and CTP bin is

$$\hat{F}_{SW,phase} = \frac{dT}{dT_{2m}}\left(\sum_{l=1}^{9}\frac{\partial c_{ice,l}}{\partial T}K_{ice,l} + \sum_{k=1}^{9}\frac{\partial c_{liq,k}}{\partial T}K_{liq,k}\right)$$

where K_{ice} and K_{liq} are the ice- and liquid-cloud kernels and the sums are performed over the τ dimension. Let K_{liq}^{*} represent the liquid-cloud kernel evaluated on the ice-cloud τ bins. The feedback can then be expressed as

$$\hat{F}_{SW,phase} = \left[\frac{dT}{dT_{2m}}\sum_{l=1}^{9}\frac{\partial c_{ice,l}}{\partial T}\left(K_{ice,l} - K_{liq,l}^{*}\right)\right]$$

$$+\left[\frac{dT}{dT_{2m}}\left(\sum_{l=1}^{9}\frac{\partial c_{ice,l}}{\partial T}K_{liq,l}^{*} + \sum_{k=1}^{9}\frac{\partial c_{liq,k}}{\partial T}K_{liq,k}\right)\right].$$

The first term in square brackets is determined by the difference between the liquid- and ice-cloud kernels, so it represents the feedback component from changes in scattering direction and the relative importance of scattering and absorption. These properties are represented by the cloud-particle asymmetry parameter g and single-scattering albedo $\widetilde{\omega}$, respectively. The second term in square brackets is determined by the difference between $\partial c_{ice}/\partial T$ and $\partial c_{liq}/\partial T$. Since $\partial c_{ice}/\partial T$ and $\partial c_{liq}/\partial T$ have opposite sign and sum to zero when adding over all τ bins, this feedback component represents changes in the overall optical depth distribution that are caused by phase changes.

All feedbacks are calculated for every latitude-month combination, except when high solar zenith angle limits the number of observations. To ensure that the cloud histograms are adequately sampled, we require that each gridbox has at least 500 valid MODIS pixels, which is 6-7% of spring and summer values. This condition is not satisfied poleward of 56°S in June and poleward of 59°S in July. In these cases, regression slopes are taken from the same latitude and the closest calendar month with sufficient data. If two months are equally close, then the average of their regression slopes is used. The feedbacks are averaged over the seasonal cycle and latitude, weighting by ocean area. Feedback uncertainty is represented by 95% confidence intervals that account for uncertainty in observed cloud-temperature relationships, uncertainty in cloud microphysical properties assumed when calculating the kernels, and inter-model spread in projections of dT_i/dT_{2m} (Appendix B).

3. Southern Ocean Cloud Feedback

We next compare the cloud-phase scattering feedback to the overall temperature-mediated feedback over the Southern Ocean. Fig. 3 shows the feedback components as a function of CTP, τ, and phase. The temperature-mediated feedback includes a vertical dipole pattern from rising upper-tropospheric ice clouds (Fig. 3a). This is qualitatively consistent with established energetic constraints: The average depth of the troposphere is limited to levels with appreciable clear-sky radiative cooling, which is constrained to temperatures warmer than ~220 K by the nature of the water-vapor rotation bands (Thompson et al., 2017; Jeevanjee and Fueglistaler, 2020). Thus, as the atmosphere warms and isotherms rise, the highest ice clouds rise as well. A second dipole pattern shows that the top of low-level liquid clouds sinks as the atmosphere warms (Fig. 3b). This cloud response has been reported in other satellite and field observations, but the physical cause is not fully understood (Huang et al., 2016; Mace et al., 2021). One possibility is that a warmer, more emissive free troposphere reduces cloud-top radiative cooling. This weakens turbulence and reduces the vertical development of boundary layer clouds (Eastman and Wood, 2018).

In contrast to the temperature-mediated feedback, the cloud-phase scattering feedback has a strikingly different pattern (Fig. 3c-d). Throughout the troposphere the ice-cloud feedback is positive and the liquid-cloud feedback is negative, indicating an ice-to-liquid conversion. The feedback magnitude maximizes in the middle troposphere, where ice and liquid clouds both occur (Fig. 1a-b). It is not obvious from Fig. 3 how much the cloud-phase scattering feedback contributes to the total temperature-mediated feedback, but it is clear that other feedback mechanisms contribute as well.

The temperature-mediated and cloud-phase feedbacks can be compared more clearly by summing the components over the CTP dimension to remove dipole signals from vertical shifts in clouds. The prevailing signal of the temperature-mediated feedback for low-level clouds (CTP $>$ 600 hPa) is an optical thinning of liquid cloud (Fig. 4a-b). Previous work suggests that this positive low-cloud optical depth feedback could be a consequence of reduced cloud-top radiative cooling, more frequent decoupling of clouds from the surface mixed layer, or more efficient drying from cloud-top entrainment (Terai et al., 2019; Mace et al., 2021). Our results do not speak to the physical cause, but they do show that the cumulative effect of positive feedback mechanisms outweighs that of negative feedback mechanisms, including enhanced condensation in saturated updrafts and cloud-phase changes (Betts and Harshvardhan, 1987; Lutsko and Cronin, 2018). Indeed, the scattering component of cloud-phase feedback is negligible for low clouds because ice clouds rarely occur at this level (Fig. 4d-e; Fig. 1).

In contrast, the feedback from non-low clouds (CTP $\leq$ 600 hPa) has different characteristics. The temperature-mediated feedback includes an ice-to-liquid conversion, and the cloud-phase scattering feedback has the same sign but larger magnitude (Fig. 4). This difference in magnitude may be associated with non-low clouds shifting upward as the atmosphere warms (Fig. 3a). As clouds shift upward they experience less warming and therefore a reduced ice-to-liquid conversion compared to what would occur if they were to remain at fixed altitudes. The estimate of cloud-phase scattering feedback represents phase conversions with fixed cloud altitudes, while the estimate of temperature-mediated feedback includes the effect of upward shifts in clouds. Despite this difference, the results consistently show that the cloud-phase scattering feedback is primarily confined to free-tropospheric clouds.

We next sum the feedback components over the optical depth dimension to determine the total feedback. Low clouds exert a significant positive temperature-mediated feedback that mostly arises from liquid clouds, and non-low clouds exert counteracting ice and liquid feedbacks that sum to a near-zero value (Fig. 4c). The low-cloud component is largest, and thus the total feedback is positive (Fig. 5a). Low clouds dominate the mean cloud albedo over the Southern Ocean, so it is perhaps not surprising that they dominate the temperature-mediated feedback as well (Haynes et al., 2011). In contrast, the cloud-phase scattering feedback is mostly limited to non-low clouds, and it consists of ice and liquid components that cancel very closely (Fig. 4f, Fig. 5a). The total temperature-mediated feedback summed over all CTP-τ-phase components is significantly positive (0.65 ± 0.32 $Wm^{-2}K^{-1}$) and is an order of magnitude larger than the total cloud-phase scattering feedback (-0.02 ± 0.05 $Wm^{-2}K^{-1}$). Thus, changes in cloud scattering properties arising from phase changes make a small contribution to the overall temperature-driven cloud feedback.

The smallness of the cloud-phase scattering feedback is surprising given that it can be much larger in model simulations (Ceppi, Hartmann, and Webb, 2016; Tan et al., 2016; Frey and Kay, 2018). To interpret this result, we decompose the feedback into contributions from changes in (1) optical depth; (2) single-scattering albedo $\widetilde{\omega}$, which is the probability that a photon-particle interaction results in scattering; and (3) asymmetry parameter g, which embodies scattering direction. The decomposition reveals that phase changes cause a negative optical depth feedback (Fig. 5b). This is consistent with the expectation that ice-to-liquid conversions reduce the average size of cloud particles, thereby increasing particle surface-area-to-volume ratio and hence the bulk optical depth. The decomposition also reveals an offsetting positive feedback from changes in g and $\widetilde{\omega}$. This component is mostly caused by changes in scattering direction: Ice particles typically backscatter more radiation than liquid droplets, so ice-to-liquid conversions enhance forward scattering and thereby reduce cloud albedo. The magnitude of this feedback component may be somewhat sensitive to the microscopic properties of cloud particles that are assumed when calculating the kernels, but the confidence intervals account for much of this uncertainty by incorporating particle-size uncertainty and using two radiative transfer schemes (Appendix B). The main interpretation is therefore robust: Ice-to-liquid conversions increase cloud optical depth and shift the scattering angles of cloud particles toward the forward direction. These counteracting feedback components make the overall cloud-phase scattering feedback small.

All of these feedback values are inferred from observed natural variability, so they are contingent on the assumptions of the methodology and the limitations of the observations. However, we tested the sensitivity of the results to the most salient of these assumptions and limitations. For instance, the radiative kernel method assumes that clouds are either entirely liquid or entirely ice (Zelinka et al., 2012) based on observed cloud-top phase. Sensitivity to this assumption is tested by matching MODIS pixels with coincident radar-lidar measurements to distinguish ice, pure liquid, and mixed-phase clouds, then estimating the cloud-phase scattering feedback while allowing for transitions between the three phase categories. We also checked sensitivity to satellite retrieval bias from high solar zenith angle and multilayer clouds, and we checked sensitivity to observing platform and time period. The envelope of feedback uncertainty from the sensitivity tests is close to that of the main estimates (Appendix C). Thus, these assumptions and limitations do not affect the main results.

4. Implications for Climate Sensitivity

We next frame the results in the context of the existing literature to show their implications for climate sensitivity. A recent survey by Sherwood et al. (2020) identified high-latitude (40°-70°) low-cloud optical depth feedback as one of six primary components of global cloud feedback. Observational studies have argued that this feedback component could be positive (Tselioudis et al., 1992; Norris and Iacobellis, 2005; Huang et al., 2016; Terai et al., 2016; Tan et al., 2019; Mace et al., 2021; Myers et al., 2021) or negative (McCoy et al., 2014b; Ceppi, McCoy, and Hartmann, 2016). Sherwood et al. (2020) therefore established a consensus estimate with a central value of 0 $Wm^{-2}K^{-1}$ and a confidence interval wide enough to include positive and negative feedback values estimated by Terai et al. (2016) and Ceppi, McCoy, and Hartmann (2016). The consensus feedback was then combined with other evidence to estimate global cloud feedback and the equilibrium response of global-mean surface temperature to doubling atmospheric CO_2. The temperature response was represented by effective climate sensitivity (Gregory et al., 2004).

Our findings support a different interpretation of high-latitude low-cloud optical depth feedback. First, we find that the feedback is positive over the Southern Ocean (0.52 ± 0.23 $Wm^{-2}K^{-1}$ over ice-free ocean between 40°-70°S). Second, we find that the negative feedback estimate on which the consensus value is based is probably biased because it does not control for the confounding influence of wind and boundary layer inversion strength (Appendix C). Third, our results rule out the possibility of a substantial negative optical depth feedback from phase changes in Southern Ocean low clouds (Fig. 4). Collectively these findings indicate that high-latitude low-cloud optical depth feedback is likely positive.

We investigate the global implications of this result using the framework of Sherwood et al. (2020). Following their analysis, we assume that the high-latitude low-cloud optical depth feedback in the Southern Hemisphere is dominated by ocean regions and is 3.8 times larger than the corresponding feedback in the Northern Hemisphere. These assumptions are based on the analysis of Terai et al. (2016). We then estimate effective climate sensitivity by performing the "Baseline" calculation of Sherwood et al. (2020) with our estimate of high-latitude low-cloud optical depth feedback in place of their consensus value. Our feedback constraint slightly narrows the probability distribution of global cloud feedback, and it increases the modal value from 0.45 $Wm^{-2}K^{-1}$ to 0.55 $Wm^{-2}K^{-1}$ (Fig. 6a). Consequently, the 66% confidence range for climate sensitivity increases from 2.55-3.88 K to 2.63-4.02 K (Fig. 6b). Our observational constraint thus shifts the bounds of the "likely" range of climate sensitivity by about +0.1 K.

5. Conclusion

Southern Ocean clouds have large radiative effects that shape global (Hwang and Frierson, 2013; Kay et al., 2016; Hawcroft et al., 2017). They are also especially difficult to simulate, so observations offer a valuable alternative path toward understanding their radiative feedbacks (Trenberth and Fasullo, 2010). Here we use MODIS observations to infer Southern Ocean SW cloud feedback as a function of cloud-top phase. The temperature-mediated feedback includes contributions from an optical thinning of low clouds and an ice-to-liquid conversion in free-tropospheric clouds (Fig. 3, Fig. 4). The low-cloud feedback dominates, causing the overall temperature-mediated feedback to be positive (Fig. 5). These constraints imply a higher climate sensitivity than a recent consensus estimate of cloud feedback (Fig. 6).

In addition to constraining SW cloud feedback, another key goal is to decompose the feedback into contributions from particular physical mechanisms. Such a decomposition is essential for understanding the climate response to external forcing. Here we leverage the new feedback methodology to isolate one mechanism: the cloud-phase scattering feedback. This mechanism increases cloud optical depth and shifts the scattering angles of cloud particles toward the forward direction. The resulting feedback components closely cancel, and thus the cloud-phase scattering feedback is an order of magnitude smaller than the overall temperature-mediated feedback (Fig. 5). These results do not preclude the possibility of a substantial cloud-phase feedback from cloud-lifetime changes (Mülmenstädt et al., 2021), nor do they reveal which mechanisms dominate the temperature-mediated feedback. However, the results do reveal a robust constraint on Southern Ocean cloud feedback: Although the dominant feedback mechanisms remain elusive, it is very unlikely that the cloud-phase scattering feedback is one of them.

Appendix A: Validation of Radiative Kernels

SW cloud radiative effect (CRE) is defined as the difference between all-sky and clear-sky SW flux at the top of the atmosphere. We validate the radiative kernels by using them to predict monthly anomalies of SW CRE:

$$\mathrm{SW\ CRE_{kernel}} = \sum_i c_i K_i \tag{3}$$

where i runs over all MODIS histogram bins, c_i is the monthly cloud-fraction anomaly reported by MODIS, and K_i is the kernel. SW $\mathrm{CRE_{kernel}}$ is compared with observed values from Clouds and the Earth's Radiant Energy System satellite data (SW $\mathrm{CRE_{CERES}}$; Loeb et al. 2018). Monthly SW CRE anomalies are averaged over one-year intervals for consistency with the annual-mean SW cloud-feedback estimates, and SW $\mathrm{CRE_{kernel}}$ is regressed on SW $\mathrm{CRE_{CERES}}$ using all data from the study domain. The regression agrees very well with conditional means of SW $\mathrm{CRE_{kernel}}$ as a function of SW $\mathrm{CRE_{CERES}}$, indicating that linear regression accurately represents bias of the kernel method (Fig. A1). If m is the regression slope, then $m - 1$ is the bias of the magnitude of SW $\mathrm{CRE_{kernel}}$. We find that $m = 1.05 \pm 0.04$ (95% confidence interval). This indicates that the kernels will overestimate the magnitude of SW cloud feedback by $5 \pm 4\%$.

Appendix B: Uncertainty

Cloud feedback is inferred from observed cloud-temperature relationships, radiative kernels, and model projections of CO_2-forced warming, so all three terms contribute to feedback uncertainty. These uncertainty components are independent, so they are calculated separately and then combined. We illustrate the uncertainty analysis by describing the calculation of the 95% confidence interval for the mean temperature-mediated feedback for both phases.

The first source of feedback uncertainty arises from uncertainty in cloud-temperature regression slopes. For a given latitude and month, the standard error of the feedback summed over all MODIS histogram bins is estimated by

$$\delta = \sqrt{\sum_i \sum_j \left(\sigma_i K_i \frac{dT_i}{dT_{2m}}\right)\left(\sigma_j K_j \frac{dT_j}{dT_{2m}}\right) r_{i,j}}$$

where i and j run over all histogram bins; σ_i is the standard error of regression slope $\partial c_i/\partial T_i$; $r_{i,j}$ is the correlation between cloud fraction in bins i and j; and dT/dT_{2m} is the CMIP6 multi-model mean value. The δ terms are combined to account for averaging over the seasonal cycle:

$$\langle\delta\rangle = \frac{1}{12}\sqrt{\sum_m \delta_m^2}$$

where m runs over all calendar months. The ⟨δ⟩ terms are then combined further to account for averaging over latitude:

$$\boldsymbol{\delta} = \sqrt{\sum_l \langle\delta\rangle_l^2 w_l^2} \Big/ \sum_l w_l$$

where l runs over all latitude bins and w_l is a weighting factor that is proportional to ocean area in bin l. Finally, the confidence interval is scaled to account for the effective degrees of freedom. Serial correlation is diagnosed from SW CRE as defined by equation (3). The ratio of nominal to effective spatial degrees of freedom, N_s/N_s^*, is calculated from equation 5 of Bretherton et al. (1999), and the ratio of nominal to effective temporal degrees of freedom is estimated by

$$N_t/N_t^* = \frac{1+r}{1-r}$$

where r is the lag-1 autocorrelation of SW CRE. N_t/N_t^* is calculated for every spatial gridpoint and then averaged. The 95% confidence interval for the mean feedback due to regression-slope uncertainty is

$$\Delta_1 = \beta\boldsymbol{\delta}\sqrt{\frac{N_s}{N_s^*}\frac{N_t}{N_t^*}}$$

where β is the critical value of a Student's t test at the 95% confidence level using $N_s^* N_t^* - 6$ degrees of freedom.

The second source of uncertainty arises from cloud microphysical properties assumed when calculating the radiative kernels. We assume a mean and 95% confidence interval for cloud-droplet effective radius of $14 \pm 3\ \mu$m, which spans the range of values throughout the climatological seasonal cycle from three MODIS-derived products (McCoy et al., 2014a). We also assume a mean and 95% confidence interval for ice-crystal effective radius of $35 \pm 10\ \mu$m based on satellite radar-lidar observations (McCoy et al., 2014a). Finally, we use two ice optical property schemes that are based on different observed particle-size distributions (Fu, 1996; Ebert and Curry, 1992). Radiative kernels are calculated with the upper and lower bounds of particle size and with both ice optical property schemes, and feedbacks are recalculated with the modified kernels. Variations in feedback values from the kernel modifications are added in quadrature to determine their cumulative contribution to cloud-feedback uncertainty, Δ_2.

The final source of uncertainty arises from the spread in model projections of CO_2-forced warming. To estimate this uncertainty we calculate feedbacks with dT/dT_{2m} from each of the 34 CMIP6 models. The second-largest and second-smallest feedback values are used as bounds for the 95% confidence interval, Δ_3.

After computing the three uncertainty terms, the 95% confidence interval for the mean temperature-mediated feedback Δ_{net} is calculated by adding the terms in quadrature:

$$\Delta_{net} = \sqrt{\Delta_1^2 + \Delta_2^2 + \Delta_3^2}.$$

Confidence intervals for other feedback components are calculated similarly.

Appendix C: Bias

Here we investigate sensitivity of the results to several assumptions of the methodology and limitations of the observations. We consider the meteorological predictors used in the regression model, the time period of analysis, and the observing platform. We also investigate satellite retrieval bias from high solar zenith angle, multilayer clouds, liquid-topped mixed-phase clouds, and partly cloudy pixels. The sensitivity tests are described below and summarized in Fig. A2.

Meteorological Predictors

Three studies including ours have reported estimates and confidence intervals for Southern Ocean SW cloud feedback inferred from MODIS data. Terai et al. (2016, hereafter T16) estimated that the mean SW low-cloud optical depth feedback between 40°-70°S is 0.38 ± 0.25 $Wm^{-2}K^{-1}$; Ceppi, McCoy, and Hartmann (2016, hereafter CMH16) estimated that the mean temperature-mediated feedback between 45°-60°S is -0.76 ± 0.82 $Wm^{-2}K^{-1}$ relative to local warming between 500-850 hPa; and we estimate that the mean temperature-mediated feedback between 40°-60°S is 0.65 ± 0.32 $Wm^{-2}K^{-1}$. The results of our study and of T16 are consistent with one another, and both are inconsistent with the results of CMH16. Here we attempt to reconcile this discrepancy.

One difference among the studies is that each one treats confounding meteorological factors differently. Our study controls for the monthly three-dimensional wind field and boundary-layer inversion strength. T16 include changes in inversion strength in their feedback estimate and screen the data for low clouds, which controls for most of the confounding influence of large-scale vertical motion. CMH16 do not control for potential confounding factors. To check if this matters, we align our analysis with that of CMH16 by estimating feedbacks using only temperature as a predictor. The temperature-only model predicts a

SW temperature-mediated feedback that is significantly more negative (Fig. A2a). Furthermore, we also check the results by applying the method of CMH16 to our cloud histograms and kernels. This yields a mean temperature-mediated feedback of -0.49 ± 0.82 Wm^{-2}K^{-1} between 45°-60°S relative to local warming between 500-850 hPa, which is consistent with the value of -0.76 ± 0.82 Wm^{-2}K^{-1} reported by CMH16. This result shows that the treatment of confounding meteorological factors is likely the main reason for the discrepancy among the studies.

The relative importance of different confounding meteorological factors can be estimated based on their correlation with temperature. For a given MODIS histogram bin i, a confounding meteorological variable x_i will bias the estimate of the temperature-mediated cloud-feedback from the temperature-only regression model by an amount F_{SW,x_i} given by

$$F_{SW,x_i} = \frac{\partial c_i}{\partial x_i}\frac{dx_i}{dT_i}K_i\frac{dT_i}{dT_{2m}}.$$

Based on this relationship, we find that estimated inversion strength and meridional wind are the two most important confounding factors. Failure to control for these variables will significantly bias the estimate of the overall temperature-mediated cloud feedback and potentially introduce a sign error. Thus, in our view, the feedback estimates of CMH16 are not reliable.

Time Period

Our analysis assumes that extratropical cloud-temperature relationships will not substantially change as the climate responds to anthropogenic radiative forcing. This assumption has been verified in many model projections of anthropogenic climate change (Gordon and Klein, 2014; Terai et al., 2016; Ceppi, McCoy, and Hartmann, 2016), though it does not hold in every model (Bjordal et al., 2020). To check the assumption further, we compare temperature-mediated feedbacks inferred from the first eight years (2003-2010) and the final eight years (2012-2019) of the 17-year MODIS record. The feedbacks inferred from the two periods are similar to one another and to the main estimate (Fig.

A2b). This provides some additional support for the assumption of time-invariant cloud-temperature relationships, at least for decadal climate changes.

Observing Platform

Our main analysis infers feedbacks using MODIS data from the Aqua satellite. We also check the results using MODIS data from the Terra satellite because MODIS-Terra is calibrated differently and acquires data in the morning rather than the afternoon. The temperature-mediated feedbacks inferred from MODIS-Aqua and MODIS-Terra are similar, so the results are not sensitive to the observing platform (Fig. A2c).

Solar Zenith Angle Bias

In addition to temporal sampling limitations, MODIS data have systematic biases that occur during certain conditions. The first bias we consider is associated with solar zenith angle (SZA). MODIS cloud retrievals assume that radiative transfer is plane parallel and that each pixel is unaffected by the radiative transfer in its surroundings. These assumptions break down when SZA $> 65°$, which biases the cloud data (Grosvenor and Wood, 2014). We investigate this bias by screening the data based on SZA. Latitude-month combinations are considered to have “good” data if SZA $< 65°$ at the data acquisition time for all pixel-level measurements, and latitude-month combinations are considered to have “mixed” data otherwise. Sensitivity to SZA bias is checked by recalculating the temperature-mediated feedback using only “good” data. Regression slopes from latitude-month combinations with “mixed” data are replaced with regression slopes from the same latitude and the closest calendar month with “good” data. When two months are equally close, then their regression slopes are averaged. The resulting feedback estimate is similar to the main estimate, indicating that SZA bias does not influence the results (Fig. A2d). This is probably because the bias does not affect data during spring and summer, when insolation is largest.

Multilayer Clouds

Other MODIS biases are especially relevant to the cloud-phase scattering feedback. For instance, the presence of multilayer clouds can cause errors in the retrievals of CTP and phase. We investigate this bias using the MODIS multilayer quality assurance flag, which identifies pixels that are suspected to be adversely affected by multilayer clouds. The proportion of cloudy scenes affected by multilayer clouds is

$$M = N_{ML}/N_{cloud}$$

where N_{ML} is the number of pixels with potentially problematic multilayer clouds and N_{cloud} is the total number of cloudy pixels. For each latitude-calendar month pairing, high-M and low-M composites are created from data with above-median and below-median values of M, respectively. The cloud-phase scattering feedback is then estimated separately for the two composites. The M difference between the high and low composites is 2.4 times smaller than the mean value of M for the whole dataset, so the high-M-minus-low-M feedback difference is scaled by a factor of 2.4 to estimate the feedback bias from multilayer clouds. Even after applying the scaling factor, the high-M-minus-low-M difference is very small (Fig. A2e). Thus, multilayer clouds do not bias the estimate of cloud-phase scattering feedback.

Liquid-topped Mixed-phase Clouds

Another data limitation that is relevant to cloud-phase feedback is the fact that MODIS retrieves phase at cloud top, so it cannot distinguish liquid-topped mixed-phase (LTMP) clouds from pure liquid clouds. Our analysis therefore treats these clouds as a single phase category. If some LTMP clouds convert to pure-liquid clouds as they warm, then the associated feedback component would not be included in our estimate of cloud-phase scattering feedback. We therefore need to estimate this component using other methods.

LTMP clouds are investigated using MODIS data and radar-lidar data from the CloudSat and CALIPSO satellites. Footprint data are analyzed from the CloudSat MOD06-1KM-AUX and 2B-CLDCLASS-LIDAR datasets from June 2006 through April 2011 (Sassen et al., 2008; Zhang et al., 2010). The radar-lidar profiles detect phase below cloud top and label clouds as either “liquid”, “ice”, or “mixed” phase. Each profile is matched with the collocated MODIS pixel and the adjacent pixel on either side in the across-track direction. MODIS pixels are then gridded by latitude, longitude, and month, and monthly cloud-fraction histograms are calculated as a function of CTP, τ, and phase.

Although radar and lidar provide valuable information, they also have sampling limitations that motivate minor methodological changes. Specifically, the radar and lidar are nadir-staring instruments, so all of the collocated MODIS pixels are viewed at nadir. These data differ from the full MODIS dataset because of viewing angle dependencies (Maddux et al., 2010). Furthermore, nadir sampling causes the number of MODIS pixels to vary by several orders of magnitude between gridboxes, which is problematic for linear regression. We accommodate this issue by calculating $\partial P_{liq}/\partial T$ by compositing. For each CTP-latitude-calendar month combination, warm and cold composites are created from the data with above-median and below-median temperature anomalies. $\partial P_{liq}/\partial T$ is then calculated from the warm-minus-cold composite difference of the mean values of P_{liq} and T weighted by the number of pixels in each gridbox. Sampling uncertainty is then estimated by bootstrapping. Data are separated into blocks with dimensions of 10° latitude, 10° longitude, and 1 month so that each block has approximately one degree of freedom. Data blocks are randomly selected with replacement to create 1000 bootstrap samples of the observations, and cloud-phase scattering feedback is estimated from each sample. The 2.5 and 97.5 percentiles of the feedback values are used as bounds for the 95% confidence interval associated with sampling uncertainty (Δ_1). All other aspects of the cloud-phase feedback methodology are carried out as before.

Fig. A2f shows cloud-phase scattering feedback estimated by this method. The first two cases show the effects of the methodological and viewing geometry differences one at a time. The “Full FOV” case is the feedback estimated using the full MODIS dataset and calculating $\partial P_{liq}/\partial T$ by compositing, and the “Nadir” case is similar except that it uses near-nadir MODIS data that are collocated with radar-lidar measurements. Feedbacks from these cases are statistically indistinguishable from one another and from the main estimate. Thus, the differences in methodology and viewing geometry do not significantly affect the results.

Having established the “Nadir” feedback, we now leverage the radar-lidar data to distinguish pure-liquid clouds from LTMP clouds. MODIS pixels that coincide with radar-lidar data are assigned to one of three phase categories: (1) “ice” when MODIS reports ice, (2) “pure liquid” when MODIS reports liquid and radar-lidar reports that the highest liquid-containing cloud is pure liquid, and (3) “LTMP” when MODIS reports liquid and radar-lidar reports that the highest liquid-containing cloud is mixed phase or that all clouds are ice. The climatology of the cloud-fraction histograms for the three phases is shown in Fig. A3. As expected from previous work, pure-liquid clouds occur most often in the boundary layer, and LTMP clouds occur most often in the middle troposphere (Zhang et al., 2010; Mace et al., 2021).

The ability to distinguish pure-liquid and LTMP clouds facilitates a revised estimate of cloud-phase scattering feedback with three phase categories. For a given CTP bin, the proportion of total cloud fraction in each phase is:

$$P_{ice} = \frac{C_{ice}}{C_{ice} + C_{pl} + C_{LTMP}}$$

$$P_{pl} = \frac{C_{pl}}{C_{ice} + C_{pl} + C_{LTMP}}$$

$$P_{LTMP} = \frac{C_{LTMP}}{C_{ice} + C_{pl} + C_{LTMP}}$$

where the subscripts “ice”, “pl”, and “LTMP” represent ice, pure liquid, and LTMP phases, respectively. We calculate $\partial C_{ice}/\partial T$, $\partial C_{pl}/\partial T$, and $\partial C_{LTMP}/\partial T$ and partition the values among the τ bins similarly to the main methodology. Finally, liquid condensate in LTMP clouds is assumed to be radiatively dominant over ice (Shupe et al., 2008), so the liquid-cloud kernel is used to calculate feedbacks for LTMP clouds. This method accounts for feedbacks that arise from phase transitions between any of the three categories, so it includes the component from LTMP-to-pure-liquid transitions that is missing from the main analysis.

The resulting feedback estimate is shown by the "Nadir w/ LTMP" case in Fig. A2f. The estimate is consistent with the first two cases and with the main estimate. Thus, the fact the MODIS is unable to distinguish LTMP clouds from pure liquid clouds does not affect the main conclusions. The vertical separation between LTMP and pure-liquid clouds is probably a key reason why the results are not sensitive to the treatment of LTMP clouds (Fig. A3).

Partly Cloudy Pixels

The final data limitation we consider is the fact that MODIS excludes partly cloudy pixels when compiling monthly histograms. This could introduce a sampling bias if cloud elements that entirely cover pixels respond to warming differently than cloud elements that partially cover pixels. Fully and partly cloudy pixels make up 70.2% and 5.9% of the observations, respectively, and the partly cloudy cases include 5.7% liquid clouds and 0.2% ice clouds. The partly cloudy pixels are probably mostly associated with the edges of liquid clouds in the boundary layer, where the estimated cloud-phase scattering feedback is small. Thus, it is unlikely that excluding partly cloudy pixels affects the estimate of cloud-phase scattering feedback.

Acknowledgements

We thank Tim Carlsen and Nick Lutsko for helpful discussions and Peter Blossey for sharing the radiative transfer code. C.J.W. was supported by the NOAA Climate and Global Change Postdoctoral Fellowship Program, administered by UCAR's Cooperative Programs for the Advancement of Earth System Science (CPAESS) under award #NA18NWS4620043B. C.J.W. and J.R.N. were also supported by NASA under grant #80NSSC18K1020.

Data and Code Availability

The datasets used in this study include (1) MODIS Collection 6 versions MYD08_M3 and MOD08_M3; (2) ERA5 reanalysis; (3) Clouds and the Earth's Radiant Energy System (CERES) Energy Balanced and Filled Edition 4.1; (4)

CloudSat data products 2B-CLDCLASS-LIDAR and MOD06-1KM-AUX version P1_R05; and (5) CMIP6 model output. These data are publicly available at https://earthdata.nasa.gov/, https://cds.climate.copernicus.eu/, https://ceres.larc.nasa.gov/data/, http://www.cloudsat.cira.colostate.edu/, and https://esgf-node.llnl.gov/projects/cmip6/, respectively. The radiative transfer model used in this study is available at http://rtweb.aer.com/rrtm_frame.html, and the code for the climate-sensitivity analysis is available at https://doi.org/10.5281/zenodo.3945276. MATLAB code used to process data is available from the corresponding author upon request. The feedback estimates are listed in Table S3 for reproducibility.

References

Armour, K., Marshall, J., Scott, J., Donohoe, A., & Newsom, E. R. (2016). Southern Ocean warming delayed by circumpolar upwelling and equatorward transport. *Nature Geoscience*, 9, 549–554. https://doi.org/10.1038/ngeo2731

Betts, A. K., and Harshvardhan (1987). Thermodynamic constraint on the cloud liquid water feedback in climate models, *Journal of Geophysical Research: Atmospheres*, 92(D7), 8483– 8485, doi:10.1029/JD092iD07p08483

Bjordal, J., Storelvmo, T., Alterskjær, K., & Carlsen, T. (2020). Equilibrium climate sensitivity above 5 °C plausible due to state-dependent cloud feedback. *Nature Geoscience*, 13, 718–721. https://doi.org/10.1038/s41561-020-00649-1

Bretherton, C. S., Widmann, M., Dymnikov, V. P., Wallace, J. M., & Bladé, I. (1999). The Effective Number of Spatial Degrees of Freedom of a Time-Varying Field. *Journal of Climate*, *12*(7), 1990-2009. https://doi.org/10.1175/1520-0442(1999)012<1990:TENOSD>2.0.CO;2

Ceppi, P., & Hartmann, D. L. (2015). Connections Between Clouds, Radiation, and Midlatitude Dynamics: a Review. *Current Climate Change Reports*, 1, 94–102. https://doi.org/10.1007/s40641-015-0010-x

Ceppi, P., Hartmann, D. L., & Webb, M. J. (2016). Mechanisms of the Negative Shortwave Cloud Feedback in Middle to High Latitudes. *Journal of Climate*, *29*(1), 139-157. https://doi.org/10.1175/JCLI-D-15-0327.1

Ceppi, P., McCoy, D. T., & Hartmann, D. L. (2016). Observational evidence for a negative shortwave cloud feedback in middle to high latitudes. *Geophysical Research Letters*, 43, 1331–1339, doi:10.1002/2015GL067499

Clough, S. A., Mlawer, E. J., Delamere, J. S., Iacono, M. J., Cady-Pereira, K., Boukabara, S., & Brown, P. D. (2004). Atmospheric radiative transfer modeling: a summary of the AER codes. *Journal of Quantitative Spectroscopy and Radiative Transfer*, 91, 233-244. https://doi.org/10.1016/j.jqsrt.2004.05.058

Eastman, R., & Wood, R. (2018). The Competing Effects of Stability and Humidity on Subtropical Stratocumulus Entrainment and Cloud Evolution from a Lagrangian Perspective, *Journal of the Atmospheric Sciences*, *75*(8), 2563-2578. https://doi.org/10.1175/JAS-D-18-0030.1

Ebert, E. E., & Curry, J. A. (1992). A parameterization of ice cloud optical properties for climate models. *Journal of Geophysical Research: Atmospheres*, 97(D4), 3831–3836, doi:10.1029/91JD02472

Frey, W. R., & Kay, J. E. (2018). The influence of extratropical cloud phase and amount feedbacks on climate sensitivity. *Climate Dynamics,* 50**,** 3097–3116 https://doi.org/10.1007/s00382-017-3796-5

Fu, Q. (1996). An Accurate Parameterization of the Solar Radiative Properties of Cirrus Clouds for Climate Models. *Journal of Climate*, *9*(9), 2058-2082. https://doi.org/10.1175/1520-0442(1996)009<2058:AAPOTS>2.0.CO;2

Gordon, N. D., & Klein, S. A. (2014). Low-cloud optical depth feedback in climate models. *Journal of Geophysical Research: Atmospheres*, 119, 6052– 6065, doi:10.1002/2013JD021052

Gregory, J. M., Ingram, W. J., Palmer, M. A., Jones, G. S., Stott, P. A., Thorpe, R. B., et al. (2004). A new method for diagnosing radiative forcing and climate sensitivity. *Geophysical Research Letters*, 31, L03205, doi:10.1029/2003GL018747

Grosvenor, D. P. & Wood, R. (2014). The effect of solar zenith angle on MODIS cloud optical and microphysical retrievals within marine liquid water clouds. *Atmospheric Chemistry and Physics*, 14, 7291–7321, https://doi.org/10.5194/acp-14-7291-2014

Hartmann, D. L. (2016). Global Physical Climatology Second Edition. Academic Press.

Hawcroft, M., Haywood, J. M., Collins, M., Jones, A., Jones, A. C., & Stephens, G. (2017). Southern Ocean albedo, inter-hemispheric energy transports and the double ITCZ: global impacts of biases in a coupled model. *Climate Dynamics* 48**,** 2279–2295. https://doi.org/10.1007/s00382-016-3205-5

Haynes, J. M., Jakob, C., Rossow, W. B., Tselioudis, G., & Brown, J. (2011). Major Characteristics of Southern Ocean Cloud Regimes and Their Effects on the Energy Budget. *Journal of Climate*, *24*(19), 5061-5080. https://doi.org/10.1175/2011JCLI4052.1

Hersbach, H., Bell, B., Berrisford, P., Hirahara, S., Horányi, A., Muñoz-Sabater, J., et al. (2020). The ERA5 global reanalysis. *Quarterly Journal of the Royal Meteorological Society*, 146, 1999– 2049. https://doi.org/10.1002/qj.3803

Huang, Y., Siems, S. T., Manton, M. J., Rosenfeld, D., Marchand, R., McFarquhar, G. M., & Protat, A. (2016). What is the Role of Sea Surface Temperature in Modulating Cloud and Precipitation Properties over the Southern Ocean? *Journal of Climate*, *29*(20), 7453-7476. https://doi.org/10.1175/JCLI-D-15-0768.1

Hwang, Y. T., & Frierson, D. M. W. (2013). Link between the double-Intertropical Convergence Zone problem and cloud biases over the Southern Ocean. *Proceedings of the National Academy of Sciences of the U.S.A.* 110(13), 4935–4940. https://doi.org/10.1073/pnas.1213302110

Jeevanjee, N., & Fueglistaler, S. (2020). Simple Spectral Models for Atmospheric Radiative Cooling. *Journal of the Atmospheric Sciences*, *77*(2), 479-497. https://doi.org/10.1175/JAS-D-18-0347.1

Kay, J. E., Wall, C. J., Yettella, V., Medeiros, B., Hannay, C., Caldwell, P., & Bitz, C. (2016). Global Climate Impacts of Fixing the Southern Ocean Shortwave Radiation Bias in the Community Earth System Model (CESM). *Journal of Climate*, *29*(12), 4617-4636. https://doi.org/10.1175/JCLI-D-15-0358.1

Loeb, N. G., Doelling, D. R., Wang, H., Su, W., Nguyen, C., Corbett, J. G., et al. (2018). Clouds and the Earth's Radiant Energy System (CERES) Energy Balanced and Filled (EBAF) Top-of-Atmosphere (TOA) Edition-4.0 Data Product. *Journal of Climate*, *31*(2), 895-918. https://doi.org/10.1175/JCLI-D-17-0208.1

Lutsko, N. J. & Cronin, T. W. (2018). Increase in precipitation efficiency with surface warming in radiative-convective equilibrium. *Journal of Advances in*

Modeling Earth Systems, 10, 2992– 3010. https://doi.org/10.1029/2018MS001482

Lutsko, N. J., Popp, M., Nazarian, R. H., & Albright, A. L. (2021). Emergent constraints on regional cloud feedbacks. *Geophysical Research Letters*, 48, e2021GL092934. https://doi.org/10.1029/2021GL092934

Mace, G. G., Protat, A., Humphries, R. S., Alexander, S. P., McRobert, I. M., Ward, J., et al. (2021). Southern Ocean cloud properties derived from CAPRICORN and MARCUS data. *Journal of Geophysical Research: Atmospheres*, 126, e2020JD033368. https://doi.org/10.1029/2020JD033368

Maddux, B. C., Ackerman, S. A., & Platnick, S. (2010). Viewing Geometry Dependencies in MODIS Cloud Products. *Journal of Atmospheric and Oceanic Technology*, *27*(9), 1519-1528. https://doi.org/10.1175/2010JTECHA1432.1

Marchant, B., Platnick, S., Meyer, K., Arnold, G. T., & Riedi, J. (2016). MODIS Collection 6 shortwave-derived cloud phase classification algorithm and comparisons with CALIOP. *Atmospheric Measurement Techniques*, 9, 1587–1599, https://doi.org/10.5194/amt-9-1587-2016

McCoy, D. T., Field, P., Bodas-Salcedo, A., Elsaesser, G. S., & Zelinka, M. D. (2020). A Regime-Oriented Approach to Observationally Constraining Extratropical Shortwave Cloud Feedbacks. *Journal of Climate*, *33*(23), 9967-9983. https://doi.org/10.1175/JCLI-D-19-0987.1

McCoy, D. T., Hartmann, D. L., & Grosvenor, D. P. (2014a). Observed Southern Ocean Cloud Properties and Shortwave Reflection. Part I: Calculation of SW Flux from Observed Cloud Properties, *Journal of Climate*, *27*(23), 8836-8857. https://doi.org/10.1175/JCLI-D-14-00287.1

McCoy, D. T., Hartmann, D. L., & Grosvenor, D. P. (2014b). Observed Southern Ocean Cloud Properties and Shortwave Reflection. Part II: Phase Changes and Low Cloud Feedback. *Journal of Climate*, *27*(23), 8858-8868. https://doi.org/10.1175/JCLI-D-14-00288.1

Mülmenstädt, J., Salzmann, M., Kay, J. E., Zelinka, M. D., Ma, P., Nam, C., et al. (2021). An underestimated negative cloud feedback from cloud lifetime changes. *Nature Climate Change*, 11, 508–513. https://doi.org/10.1038/s41558-021-01038-1

Myers, T. A., Scott, R. C., Zelinka, M. D., Klein, S. A., Norris, J. R., & Caldwell, P. M. (2021). Observational constraints on low cloud feedback reduce uncertainty of climate sensitivity. *Nature Climate Change*, 11, 501–507. https://doi.org/10.1038/s41558-021-01039-0

Norris, J. R., & Iacobellis, S. F. (2005). North Pacific Cloud Feedbacks Inferred from Synoptic-Scale Dynamic and Thermodynamic Relationships. *Journal of Climate*, *18*(22), 4862-4878. https://doi.org/10.1175/JCLI3558.1

Platnick, S., Meyer, K., King, M. D., Wind, G., Amarasinghe, N., Marchant, B., et al. (2017). The MODIS Cloud Optical and Microphysical Products: Collection 6 Updates and Examples From Terra and Aqua. *IEEE Transactions on Geoscience and Remote Sensing*, 55(1), 502-525, doi:10.1109/TGRS.2016.2610522

Sassen, K., Wang, Z., & Liu, D. (2008). Global distribution of cirrus clouds from CloudSat/Cloud-Aerosol Lidar and Infrared Pathfinder Satellite Observations (CALIPSO) measurements. *Journal of Geophysical Research: Atmospheres*, 113, D00A12, doi:10.1029/2008JD009972

Scott, R. C., Myers, T. A., Norris, J. R., Zelinka, M. D., Klein, S. A., Sun, M., & Doelling, D. R. (2020). Observed Sensitivity of Low-Cloud Radiative Effects to Meteorological Perturbations over the Global Oceans. *Journal of Climate*, *33*(18), 7717-7734. https://doi.org/10.1175/JCLI-D-19-1028.1

Sherwood, S. C., Webb, M. J., Annan, J. D., Armour, K. C., Forster, P. M., Hargreaves, J. C., et al. (2020). An assessment of Earth's climate sensitivity using multiple lines of evidence. *Reviews of Geophysics*. 58, e2019RG000678. https://doi.org/10.1029/2019RG000678

Shupe, M. D., Daniel, J. S., de Boer, G., Eloranta, E. W., Kollias, P., Long, C. N., et al. (2008). A Focus On Mixed-Phase Clouds, *Bulletin of the American Meteorological Society*, *89*(10), 1549-1562. https://doi.org/10.1175/2008BAMS2378.1

Stackhouse, P. W., Jr., & Stephens, G. L. (1991). A Theoretical and Observational Study of the Radiative Properties of Cirrus: Results from FIRE 1986. *Journal of Atmospheric Sciences*, *48*(18), 2044-2059. https://doi.org/10.1175/1520-0469(1991)048<2044:ATAOSO>2.0.CO;2

Storelvmo, T., Tan, I., & Korolev, A. V. (2015). Cloud Phase Changes Induced by CO_2 Warming—a Powerful yet Poorly Constrained Cloud-Climate Feedback. *Current Climate Change Reports,* 1**,** 288–296. https://doi.org/10.1007/s40641-015-0026-2

Tan, I., Oreopoulos, L., & Cho, N. (2019). The role of thermodynamic phase shifts in cloud optical depth variations with temperature. *Geophysical Research Letters*, 46, 4502– 4511. https://doi.org/10.1029/2018GL081590

Tan, I., Storelvmo, T., & Zelinka, M. D. (2016). Observational constraints on mixed-phase clouds imply higher climate sensitivity. *Science*, 352, 224-227. doi:10.1126/science.aad5300

Terai, C. R., Zelinka, M., & Klein, S. A. (2016). Constraining the low-cloud optical depth feedback at middle and high latitudes using satellite observations. *Journal of Geophysical Research: Atmospheres*, 121, 9696–9716, doi:10.1002/2016JD025233

Terai, C. R., Zhang, Y., Klein, S. A., Zelinka, M. D., Chiu, J. C., & Min, Q. (2019). Mechanisms behind the extratropical stratiform low-cloud optical depth response to temperature in ARM site observations, *Journal of Geophysical Research: Atmospheres*, 124, 2127– 2147. https://doi.org/10.1029/2018JD029359

Thompson, D. W. J., Bony, S., & Li, W. (2017). Thermodynamic constraint on the depth of the global tropospheric circulation. *Proceedings of the National Academy of Sciences of the USA*, 114, 8181-8186. https://doi.org/10.1073/pnas.1620493114

Trenberth, K. E., & Fasullo, J. T. (2010). Simulation of Present-Day and Twenty-First-Century Energy Budgets of the Southern Oceans. *Journal of Climate*, *23*(2), 440-454. https://doi.org/10.1175/2009JCLI3152.1

Tselioudis, G., DelGenio, A. D., Kovari, W., Jr., & Yao, M. (1998). Temperature Dependence of Low Cloud Optical Thickness in the GISS GCM: Contributing Mechanisms and Climate Implications. *Journal of Climate*, *11*(12), 3268-3281. https://doi.org/10.1175/1520-0442(1998)011<3268:TDOLCO>2.0.CO;2

Tselioudis, G., Rossow, W. B., & Rind, D. (1992). Global Patterns of Cloud Optical Thickness Variation with Temperature, *Journal of Climate*. *5*(12), 1484-1495. https://doi.org/10.1175/1520-0442(1992)005<1484:GPOCOT>2.0.CO;2

Wood, R., & Bretherton, C. S. (2006). On the Relationship between Stratiform Low Cloud Cover and Lower-Tropospheric Stability. *Journal of Climate*, *19*(24), 6425-6432. https://doi.org/10.1175/JCLI3988.1

Zelinka, M. D., Klein, S. A., & Hartmann, D. L. (2012). Computing and Partitioning Cloud Feedbacks Using Cloud Property Histograms. Part I: Cloud Radiative Kernels. *Journal of Climate*, *25*(11), 3715-3735. https://doi.org/10.1175/JCLI-D-11-00248.1

Zelinka, M. D., Myers, T. A., McCoy, D. T., Po-Chedley, S., Caldwell, P. M., Ceppi, P., et al. (2020). Causes of higher climate sensitivity in CMIP6 models. *Geophysical Research Letters*, 47, e2019GL085782. https://doi.org/10.1029/2019GL085782

Zhang, D., Wang, Z., & Liu, D. (2010). A global view of midlevel liquid-layer topped stratiform cloud distribution and phase partition from CALIPSO and CloudSat measurements. *Journal of Geophysical Research: Atmospheres*, 115, D00H13, doi:10.1029/2009JD012143

Figures

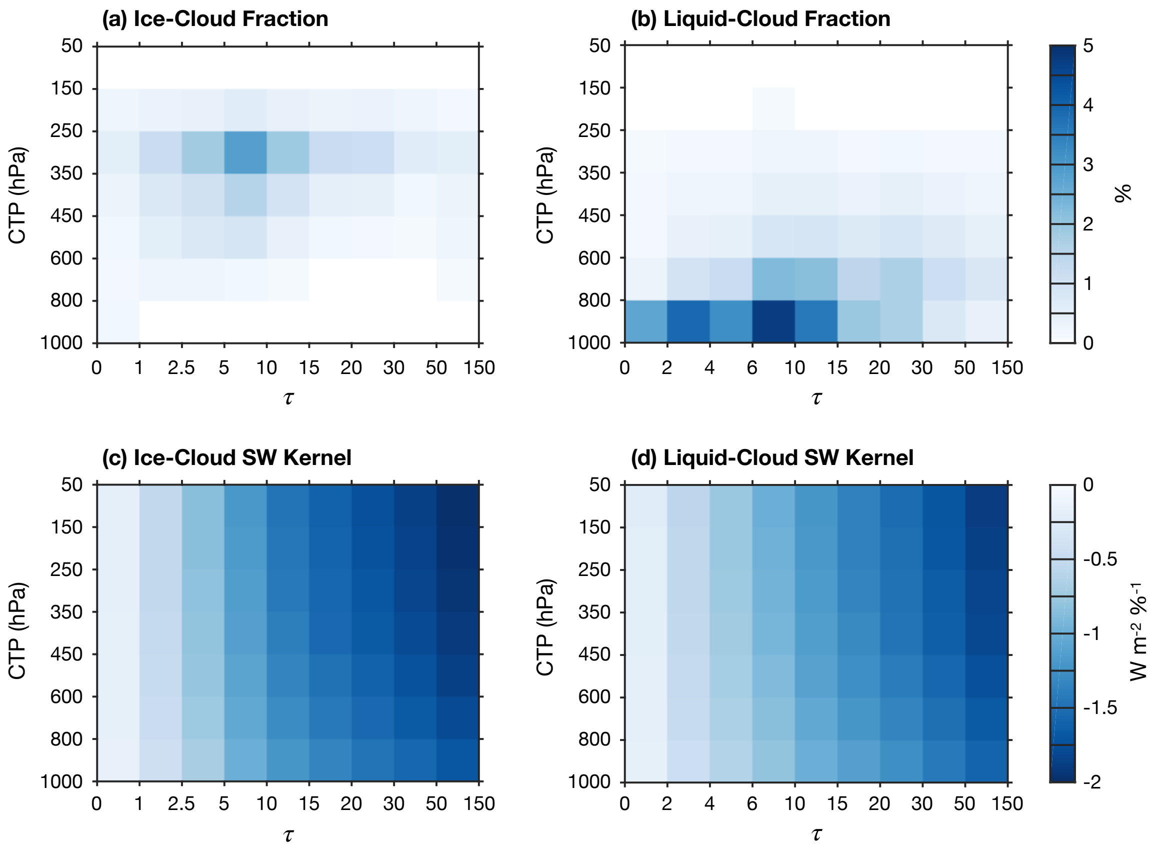

Figure 1. Climatology of cloud fraction and SW cloud radiative kernels over the Southern Ocean. Ice- and liquid-cloud fraction are shown in (a-b), and the ice- and liquid-cloud kernels are shown in (c-d).

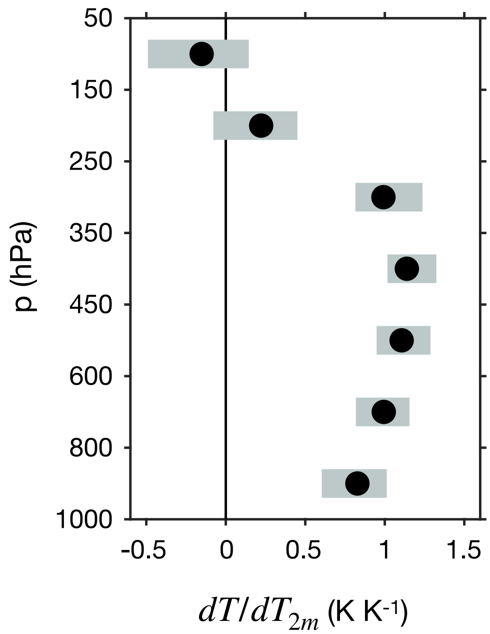

Figure 2. Ratio of atmospheric warming over the Southern Ocean to global-mean surface warming from CMIP6 projections forced by increasing atmospheric CO_2 (dT/dT_{2m}). The plotted values are spatial and temporal averages. Black dots show the multi-model mean, and gray bars show the inter-model range.

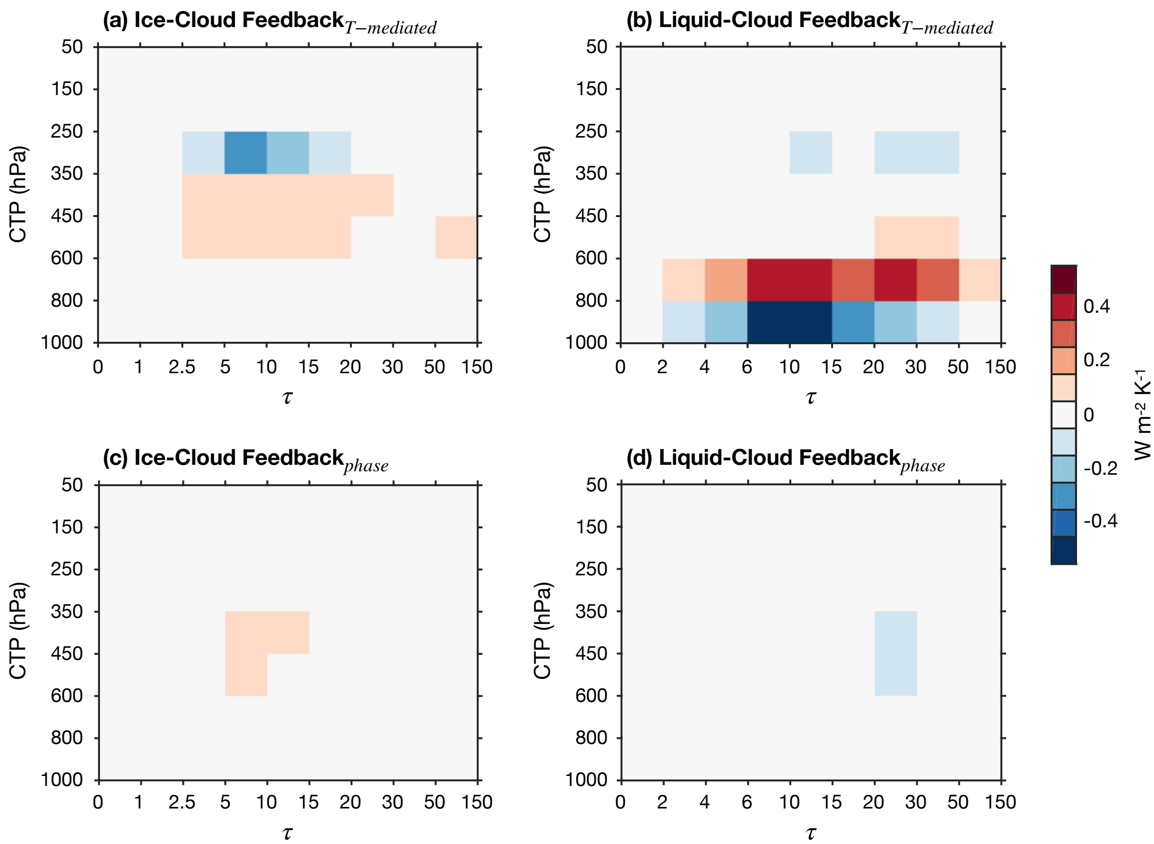

Figure 3. Southern Ocean SW cloud feedback as a function of cloud-top pressure (CTP), optical depth (τ), and phase. The temperature-mediated feedback is shown in (a-b), and the cloud-phase scattering feedback is shown in (c-d).

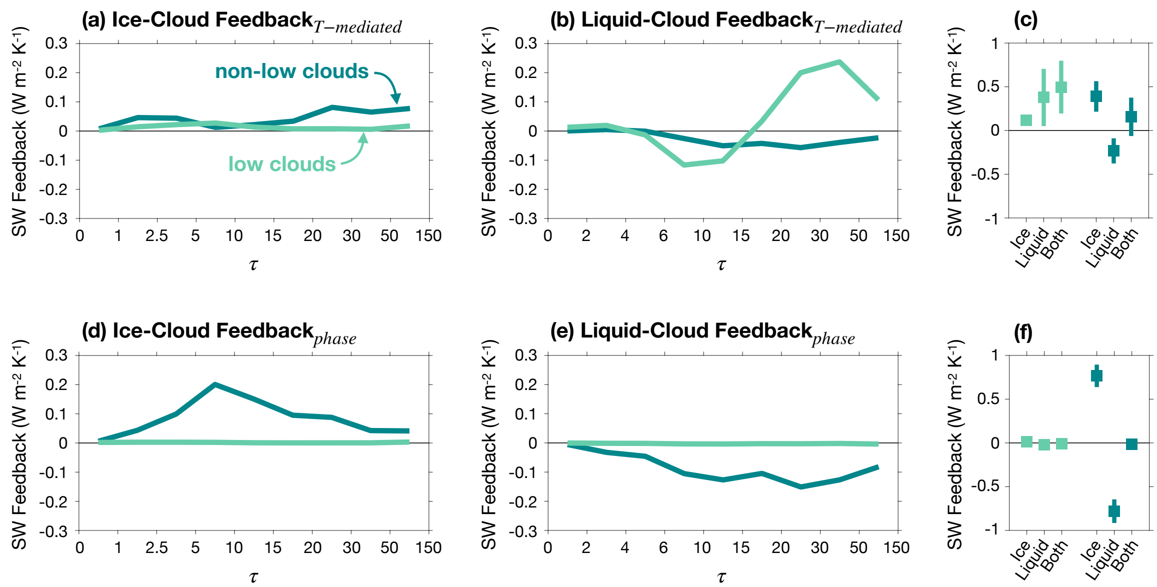

Figure 4. SW feedbacks from low clouds (CTP > 600 hPa) and non-low clouds (CTP ≤ 600 hPa). (a-b) Ice- and liquid-cloud components of the temperature-mediated feedback as a function of optical depth (τ). (c) Feedback components summed over the τ dimension. The sum of the liquid- and ice-cloud components is labeled “Both”. Squares and lines show the mean and 95% confidence interval. (d-f) As in (a-c), but for the cloud-phase scattering feedback.

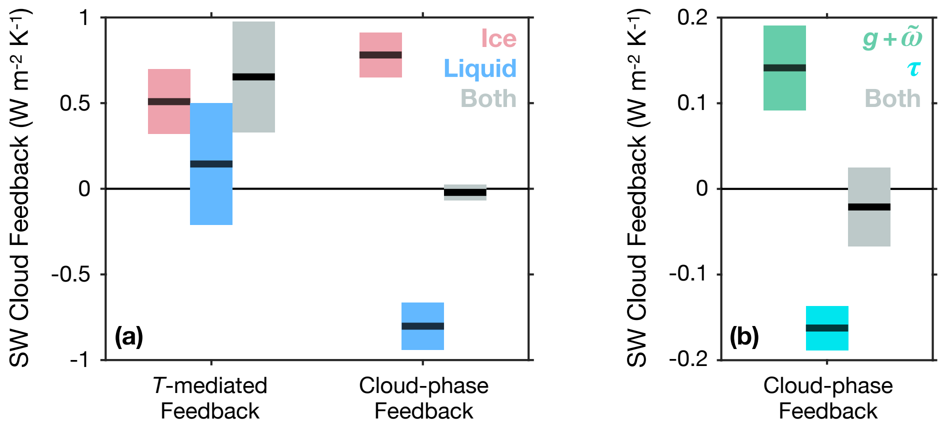

Figure 5. Mean SW cloud feedback over the Southern Ocean. (a) Temperature-mediated feedback and cloud-phase scattering feedback for ice clouds, liquid clouds, and both phases combined. Lines and colored bars show the mean and 95% confidence interval. (b) Cloud-phase scattering feedback decomposed into contributions from changes in cloud asymmetry parameter and single-scattering albedo ($g + \tilde{\omega}$) and optical depth (τ).

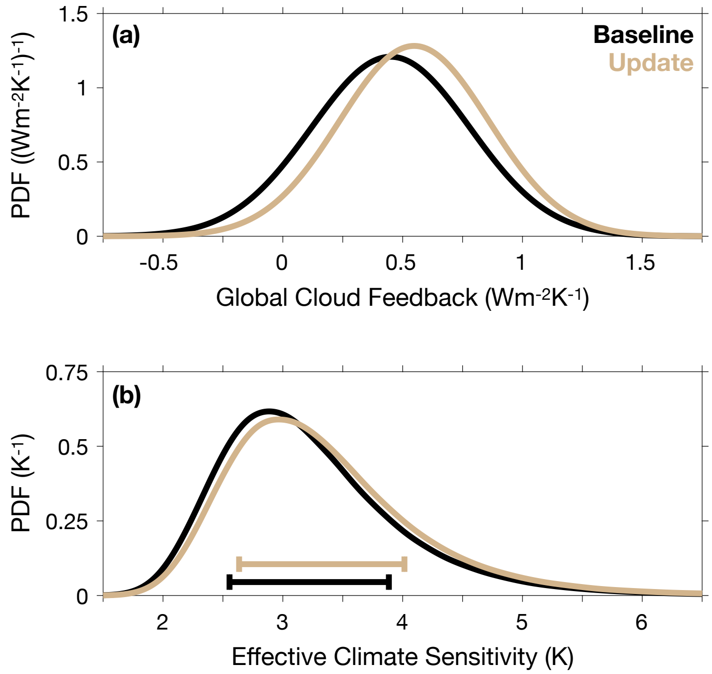

Figure 6. Implications of the feedback constraints for climate sensitivity. The "Baseline" case shows values from a survey by Sherwood et al. (2020), and the "Update" case is similar except that it uses our estimate of high-latitude low-cloud optical depth feedback. Probability density functions (PDF) are shown for (a) global cloud feedback and (b) effective climate sensitivity. Horizontal lines in (b) show the 66% confidence range.

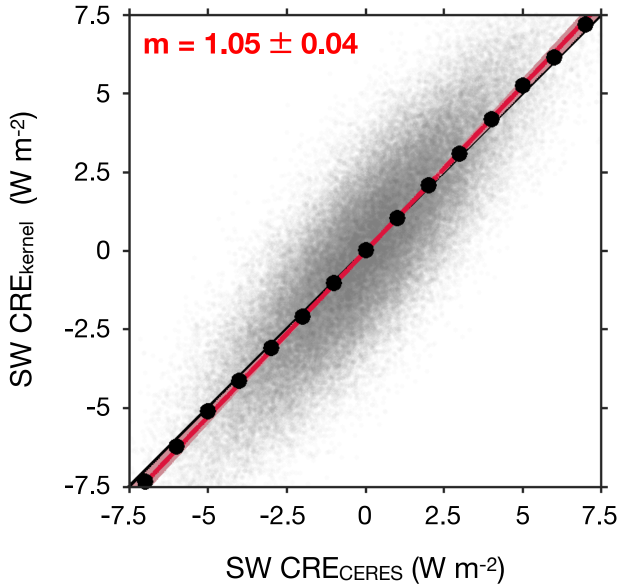

Figure A1. Validation of the radiative kernels. Kernel-predicted SW cloud radiative effect (SW CRE$_{kernel}$) is plotted as function of observed SW cloud radiative effect (SW CRE$_{CERES}$). Grey dots are individual data points, and black dots are conditional means of SW CRE$_{kernel}$ as a function of SW CRE$_{CERES}$. The red line and shading show the regression line and its 95% confidence interval. The regression slope is in the top left corner.

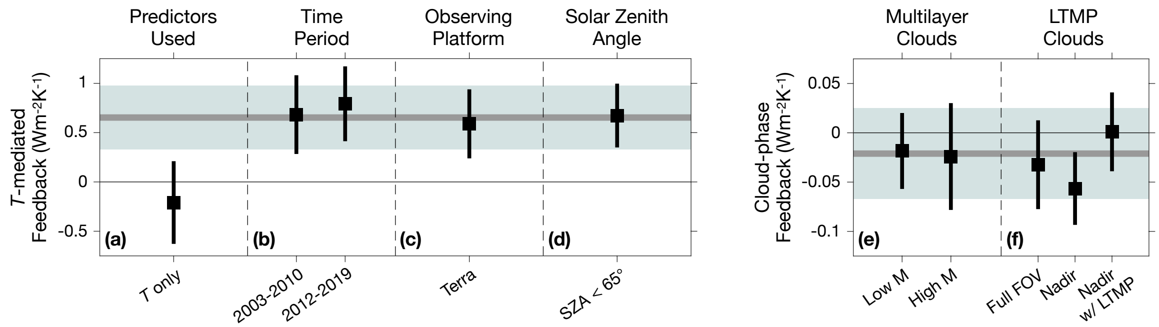

Figure A2. Summary of the sensitivity tests. Panels (a-d) show the temperature-mediated cloud feedback, and panels (e-f) show the cloud-phase scattering feedback. The values represent feedbacks from all cloud phases combined. Gray lines and shading show the mean and 95% confidence interval for the main estimate, and black squares and lines show the mean and 95% confidence interval for the sensitivity tests. (a) Sensitivity to excluding meteorological predictors. The “T only” case estimates the feedback using only temperature as a predictor. (b) Sensitivity to time period. The “2003-2010” and “2012-2019” cases estimate feedbacks using the earliest and latest eight-year periods of the record. (c) Sensitivity to observing platform. The “Terra” case estimates the feedback using data from the Terra satellite. (d) Sensitivity to bias from high solar zenith angle (SZA). The “SZA $<$ 65°” case estimates the feedback using MODIS data that are not affected by bias from high SZA. (e) Sensitivity to multilayer clouds. The “Low M” and “High M” cases estimate feedbacks using subsets that have relatively low and high proportions of data with suspected multilayer-cloud bias. (f) Sensitivity to the treatment of liquid-topped mixed-phase clouds (LTMP). The “Full FOV” case estimates the feedback using the full MODIS dataset and applying the compositing technique that is introduced to accommodate radar-lidar data (see text). The “Nadir” case is similar but uses the near-nadir subset of MODIS pixels that are collocated with radar-lidar measurements. The “Nadir w/ LTMP” case is similar to the “Nadir” case except that the feedback is estimated using three phase categories: “ice”, “pure liquid”, and “LTMP”.

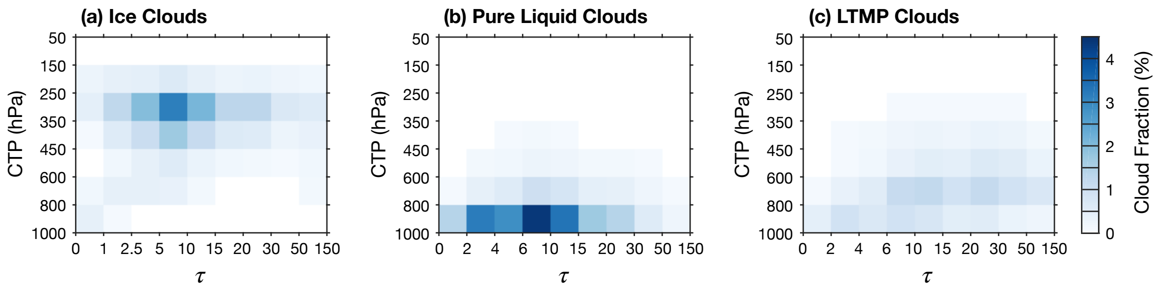

Figure A3. Climatology of cloud fraction over the Southern Ocean from MODIS data that are collocated with radar-lidar measurements from the CloudSat and CALIPSO satellites. Panels (a-c) show ice, pure liquid, and liquid-topped mixed-phase (LTMP) clouds, respectively.